

Crossed Nonlinear Dynamical Hall Effect in Twisted Bilayers

Cong Chen,^{1,2,*} Dawei Zhai,^{1,2,*} Cong Xiao,^{1,2,†} and Wang Yao^{1,2,‡}

¹*Department of Physics, The University of Hong Kong, Hong Kong, China*

²*HKU-UCAS Joint Institute of Theoretical and Computational Physics at Hong Kong, China*

We propose an unconventional nonlinear dynamical Hall effect characteristic of twisted bilayers. The joint action of in-plane and out-of-plane ac electric fields generates Hall currents $\mathbf{j} \sim \dot{\mathbf{E}}_{\perp} \times \mathbf{E}_{\parallel}$ in both sum and difference frequencies, and when the two orthogonal fields have common frequency their phase difference controls the on/off, direction and magnitude of the rectified dc Hall current. This novel intrinsic Hall response has a band geometric origin in the momentum space curl of interlayer Berry connection polarizability, arising from layer hybridization of electrons by the twisted interlayer coupling. The effect allows a unique rectification functionality and a transport probe of chiral symmetry in bilayer systems. We show sizable effects in twisted homobilayer transition metal dichalcogenides and twisted bilayer graphene over broad range of twist angles.

Nonlinear Hall-type response to an in-plane electric field in a two dimensional (2D) system with time reversal symmetry has attracted marked interests [1–4]. Intensive studies have been devoted to uncovering new types of nonlinear Hall transport induced by quantum geometry [4–6] and their applications such as terahertz rectification [7] and magnetic information readout [8]. Restricted by symmetry [1], the known mechanisms of nonlinear Hall response in quasi-2D nonmagnetic materials [2, 3, 9, 10] are all of extrinsic nature, sensitive to fine details of disorders [11, 12], which have limited their utilization for practical applications. Moreover, having a single driving field only, the effect has not unleashed the full potential of nonlinearity for enabling controlled gate in logic operation, where separable inputs (i.e., in orthogonal directions) are desirable. The latter, in the context of Hall effect, calls for control by both out-of-plane and in-plane electric fields.

A strategy to introduce quantum geometric response to out-of-plane field in quasi-2D geometry is made possible in van der Waals (vdW) layered structures with twisted stacking [13–19]. Taking homobilayer as an example, electrons have an active layer degree of freedom that is associated with an out-of-plane electric dipole [20, 21], whereas interlayer quantum tunneling rotates this pseudospin about in-plane axes that are of topologically nontrivial textures in the twisted landscapes [22–24]. Such layer pseudospin structures can underlie novel quantum geometric properties when coupled with out-of-plane field. Recent studies have found layer circular photogalvanic effect [25] and layer-contrasted time-reversal-even Hall effect [26], arising from band geometric quantities.

In this work we unveil a new type of nonlinear Hall effect in time-reversal symmetric twisted bilayers, where an intrinsic Hall current emerges under the combined action of an in-plane electric field \mathbf{E}_{\parallel} and an out-of-plane ac field $\mathbf{E}_{\perp}(t)$: $\mathbf{j} \sim \dot{\mathbf{E}}_{\perp} \times \mathbf{E}_{\parallel}$ [see Fig. 1(a)]. Having the two driving fields (inputs) and the current response (output) all orthogonal to each other, the effect is dubbed as

the *crossed nonlinear dynamical Hall effect*. This is also the first nonlinear Hall contribution of an intrinsic nature in nonmagnetic materials without external magnetic field, determined solely by the band structures, not relying on extrinsic factors such as disorders and relaxation times. The effect arises from the interlayer hybridization of electronic states under the chiral crystal symmetry characteristic of twisted bilayers, and has a novel band geometric origin in the momentum space curl of interlayer Berry connection polarizability (BCP). Having two driving fields of the same frequency, a *dc* Hall current develops, whose on/off, direction and magnitude can all be controlled by the phase difference of the two fields, which does not affect the magnitude of the double-frequency component. Such a characteristic tunability renders this effect a unique approach to rectification and transport probe of chiral bilayers. As examples, we show sizable effects in small angle twisted transition metal dichalcogenides (tTMDs) and twisted bilayer graphene (tBG), as well as tBG of large angles where Umklapp interlayer tunneling dominates.

Geometric origin of the effect. A bilayer system couples to in-plane and out-of-plane driving electric fields in completely different ways. The in-plane field couples to the 2D crystal momentum, leading to Berry-phase effects in the 2D momentum space [27]. In comparison, the out-of-plane field is coupled to the interlayer dipole moment \hat{p} in the form of $-E_{\perp}\hat{p}$, where $\hat{p} = ed_0\hat{\sigma}_z$ with $\hat{\sigma}_z$ as the Pauli matrix in the layer index subspace and d_0 the interlayer distance. When the system has a more than twofold rotational axis in the z direction, as in tBG and tTMDs, any in-plane current driven by the out-of-plane field alone is forbidden. It also prohibits the off-diagonal components of the symmetric part of the conductivity tensor $\sigma_{ab} = \partial j_a / \partial E_{\parallel,b}$ with respect to the in-plane input and output. Since the antisymmetric part of σ_{ab} is not allowed by the Onsager reciprocity in nonmagnetic systems, all the off-diagonal components of σ_{ab} is forbidden, irrespective of the order of out-of-plane field. On the other hand, as we will show, an in-plane Hall conductivity $\sigma_{xy} = -\sigma_{yx}$ can still be driven by the product

of an in-plane field and the time variation rate of an out-of-plane ac field, which is a characteristic effect of chiral bilayers.

To account for the effect, we make use of the semi-classical theory [27–30]. The velocity of an electron in a bilayer system is given by

$$\dot{\mathbf{r}} = \frac{1}{\hbar} \partial_{\mathbf{k}} \tilde{\varepsilon} - \frac{e}{\hbar} \mathbf{E}_{\parallel} \times \boldsymbol{\Omega}_{\mathbf{k}} - \boldsymbol{\Omega}_{\mathbf{k}E_{\perp}} \dot{E}_{\perp}, \quad (1)$$

where $\hbar \mathbf{k}$ is the 2D crystal momentum. Here and hereafter we suppress the band index for simplicity, unless otherwise noted. The three contributions in this equation come from the band velocity, the anomalous velocities induced by the k -space Berry curvature $\boldsymbol{\Omega}_{\mathbf{k}}$ and by the hybrid Berry curvature $\boldsymbol{\Omega}_{\mathbf{k}E_{\perp}}$ in the (\mathbf{k}, E_{\perp}) space.

For the velocity at the order of interest, the k -space Berry curvature is corrected to the first order of the variation rate of out-of-plane field \dot{E}_{\perp} as

$$\boldsymbol{\Omega}_{\mathbf{k}} = \partial_{\mathbf{k}} \times (\mathcal{A} + \mathcal{A}^{\dot{E}_{\perp}}). \quad (2)$$

Here $\mathcal{A} = \langle u_{\mathbf{k}} | i \partial_{\mathbf{k}} | u_{\mathbf{k}} \rangle$ is the unperturbed k -space Berry connection, with $|u_{\mathbf{k}}\rangle$ being the cell-periodic part of the Bloch wave, whereas

$$\mathcal{A}^{\dot{E}_{\perp}}(\mathbf{k}) = \mathcal{G}(\mathbf{k}) \dot{E}_{\perp} \quad (3)$$

is its gauge invariant correction [27, 31, 32], which can be identified physically as an in-plane positional shift of an electron [28, 33, 34] induced by the time evolution of the out-of-plane field. For a band with index n , we have

$$\mathcal{G}^n(\mathbf{k}) = 2\hbar^2 \text{Re} \sum_{m \neq n} \frac{p^{nm}(\mathbf{k}) v^{mn}(\mathbf{k})}{[\varepsilon_n(\mathbf{k}) - \varepsilon_m(\mathbf{k})]^3}, \quad (4)$$

whose numerator involves the interband matrix elements of the interlayer dipole and velocity operators, and ε_n is the unperturbed band energy. Meanwhile, up to the first order of in-plane field, the hybrid Berry curvature reads $\boldsymbol{\Omega}_{\mathbf{k}E_{\perp}} = \partial_{\mathbf{k}} (\mathfrak{A} + \mathfrak{A}^{E_{\parallel}}) - \partial_{E_{\perp}} (\mathcal{A} + \mathcal{A}^{E_{\parallel}})$. Here $\mathcal{A}^{E_{\parallel}}$ is the k -space Berry connection induced by E_{\parallel} field [28, 30], which represents an intralayer positional shift and whose detailed expression is not needed for our purpose. $\mathfrak{A} = \langle u_{\mathbf{k}} | i \partial_{E_{\perp}} | u_{\mathbf{k}} \rangle$ is the E_{\perp} -space Berry connection [25], and

$$\mathfrak{A}^{E_{\parallel}}(\mathbf{k}) = \frac{e}{\hbar} \mathcal{G}(\mathbf{k}) \cdot \mathbf{E}_{\parallel} \quad (5)$$

is its first order correction induced by the in-plane field. In addition, $\tilde{\varepsilon} = \varepsilon + \delta\varepsilon$, where $\delta\varepsilon = e \mathbf{E}_{\parallel} \cdot \mathcal{G} \dot{E}_{\perp}$ is the field-induced electron energy [29].

Given that $\mathfrak{A}^{E_{\parallel}}$ is the E_{\perp} -space counterpart of intralayer shift $\mathcal{A}^{E_{\parallel}}$, and that E_{\perp} is conjugate to the interlayer dipole moment, we can pictorially interpret $\mathfrak{A}^{E_{\parallel}}$ as the interlayer shift induced by in-plane field. It indeed has the desired property of flipping sign under the horizontal mirror-plane reflection, hence is analogous to

the so-called interlayer coordinate shift introduced in the study of layer circular photogalvanic effect [25], which is nothing but the E_{\perp} -space counterpart of the shift vector well known in the nonlinear optical phenomenon of shift current. Therefore, the E_{\perp} -space BCP $e\mathcal{G}/\hbar$ can be understood as the interlayer BCP. This picture is further augmented by the connotation that the interlayer BCP is featured exclusively by interlayer-hybridized electronic states: According to Eq. (4), if the state $|u_n\rangle$ is fully polarized in a specific layer around some momentum \mathbf{k} , then $\mathcal{G}(\mathbf{k})$ is suppressed.

With the velocity of individual electrons, the charge current density contributed by the electron system can be obtained from

$$\mathbf{j} = e \int [d\mathbf{k}] f_0 \dot{\mathbf{r}}, \quad (6)$$

where $[d\mathbf{k}]$ is shorthand for $\sum_n d^2\mathbf{k}/(2\pi)^2$, and the distribution function is taken to be the Fermi function f_0 as we focus on the intrinsic response. The band geometric contributions to $\dot{\mathbf{r}}$ lead to a Hall current

$$\mathbf{j} = \chi^{\text{int}} \dot{\mathbf{E}}_{\perp} \times \mathbf{E}_{\parallel}, \quad (7)$$

where

$$\chi^{\text{int}} = \frac{e^2}{\hbar} \int [d\mathbf{k}] f_0 [\partial_{\mathbf{k}} \times \mathcal{G}(\mathbf{k})]_z \quad (8)$$

is intrinsic to the band structure. This band geometric quantity measures the k -space curl of the interlayer BCP over the occupied states, and hence is also a characteristic of layer-hybridized electronic states. Via an integration by parts, it becomes clear that χ^{int} is a Fermi surface property. Since χ^{int} is a time-reversal even pseudoscalar, it is invariant under rotation, but flips sign under space inversion, mirror reflection and roto-reflection symmetries. As such, χ^{int} is allowed if and only if the system possesses a chiral crystal structure, which is the very case of twisted bilayers [25, 26]. Moreover, since twisted structures with opposite twist angles are mirror images of each other, whereas the mirror reflection flips the sign of χ^{int} , the direction of Hall current can be reversed by reversing twist direction.

Hall rectification and frequency doubling. This effect can be utilized for the rectification and frequency doubling of an in-plane ac input $\mathbf{E}_{\parallel} = \mathbf{E}_{\parallel}^0 \cos \omega t$, provided that the out-of-plane field has the same frequency, namely $E_{\perp} = E_{\perp}^0 \cos(\omega t + \varphi)$. The phase difference φ between the two fields plays an important role in determining the Hall current, which takes the form of

$$\mathbf{j} = \mathbf{j}^0 \sin \varphi + \mathbf{j}^{2\omega} \sin(2\omega t + \varphi). \quad (9)$$

Here ω is required to be below the threshold for direct interband transition in order to validate the semiclassical treatment, and

$$\mathbf{j}^0 = \mathbf{j}^{2\omega} = \sigma_{\text{H}} \hat{\mathbf{z}} \times \mathbf{E}_{\parallel}^0 \quad \text{with} \quad \sigma_{\text{H}} = \frac{1}{2} \omega E_{\perp}^0 \chi^{\text{int}}. \quad (10)$$

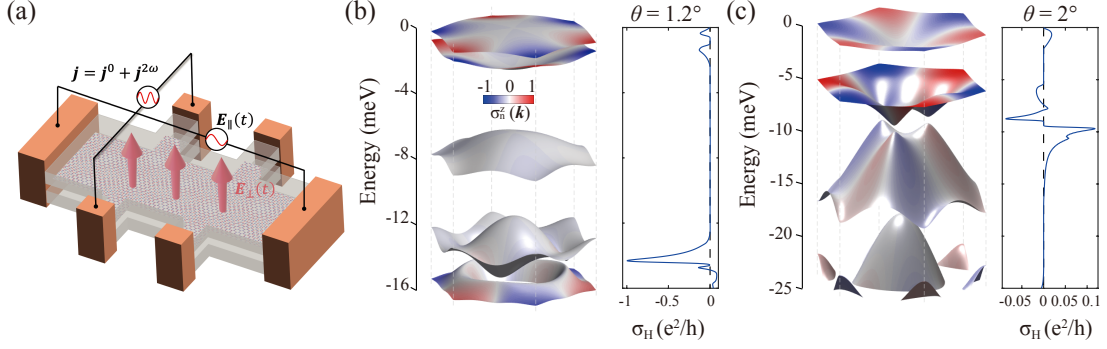


FIG. 1. (a) Schematics of experimental setup. (b, c) Valence band structure and intrinsic Hall conductivity with respect to in-plane input for tMoTe₂ at twist angles (b) $\theta = 1.2^\circ$ and (c) $\theta = 2^\circ$ in +K valley. Color coding in (b) and (c) denotes the layer composition $\sigma_n^z(\mathbf{k})$.

σ_H has the dimension of conductance and quantifies the Hall response with respect to the in-plane input. In experiment, the Hall output by the crossed nonlinear dynamic Hall effect can be distinguished readily from the conventional nonlinear Hall effect driven by in-plane field alone, as they are odd and even, respectively, in the in-plane field.

One notes that while the double-frequency component appears for any φ , the rectified output is allowed only if the two crossed driving fields are not in-phase or anti-phase. Its on/off, chirality (right or left), and magnitude are all controlled by the phase difference of the two fields. Such a unique tunability provides not only a prominent experimental hallmark of this effect, but also a controllable route to Hall rectification. In addition, reversing the direction of the out-of-plane field switches that of the Hall current, which also serves as a control knob.

Application to tTMDs. We now study the effect quantitatively in tTMDs, using tMoTe₂ as an example [22, 23] (see details of the continuum model in [26]). For illustrative purposes, we take $\omega/2\pi = 0.1$ THz and $E_\perp^0 d_0 = 10$ mV [13, 18, 19] in what follows.

Figures 1(b) and (c) present the electronic band structures along with the layer composition $\sigma_n^z(\mathbf{k})$ at twist angles $\theta = 1.2^\circ$ and $\theta = 2^\circ$. In both cases, the energy spectra exhibit isolated narrow bands with strong layer hybridization. At $\theta = 1.2^\circ$, the conductivity shows two peaks $\sim 0.1e^2/h$ at low energies associated with the first two valence bands. The third band does not host any sizable conductivity signal. At higher hole-doping levels, a remarkable conductivity peak $\sim e^2/h$ appears near the gap separating the fourth and fifth bands. At $\theta = 2^\circ$, the conductivity shows smaller values, but the overall trends are similar: A peak $\sim \mathcal{O}(0.01)e^2/h$ appears at low energies, while larger responses $\sim \mathcal{O}(0.1)e^2/h$ can be spotted as the Fermi level decreases.

One can understand the behaviors of σ_H from the interlayer BCP in Eq. (4). It favors band near-degeneracy regions in k -space made up of strongly layer hybridized electronic states. As such, the conductivity is most pro-

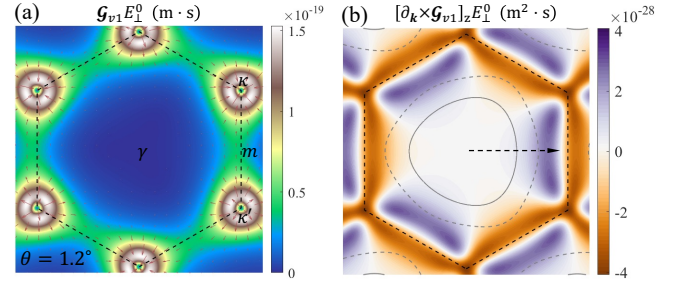


FIG. 2. (a) The interlayer BCP \mathcal{G} , and (b) its vorticity $[\partial_{\mathbf{k}} \times \mathcal{G}]_z$ on the first valence band from +K valley of 1.2° tMoTe₂. Background color and arrows in (a) denote the magnitude and vector flow, respectively. Grey curves in (b) show energy contours at 1/2 and 3/4 of the band width. The black dashed arrow denotes direction of increasing hole doping level. Black dashed hexagons in (a, b) denote the boundary of moiré Brillouin zone (mBZ).

nounced when the Fermi level is located around such regions, which directly accounts for the peaks of response in Fig. 1(b) [and 1(c)]. When the Fermi level is located on the third valence band in Fig. 1(b), the effect is vanishingly small due to the large gaps to adjacent bands.

Let us take the case of Fermi level being located within the first valence band in Fig. 1(b) as an example and explain the emergence of the first peak of conductivity. The k -space distributions of \mathcal{G} and $[\partial_{\mathbf{k}} \times \mathcal{G}]_z$ for the first valence band of 1.2° tMoTe₂ are shown in Figs. 2(a) and 2(b), respectively. \mathcal{G} is suppressed around the corners of mBZ, for the states are strongly layer polarized there. Interlayer hybridization becomes stronger as \mathbf{k} moves away from mBZ corners. In this process, the competition between enlarged $p^{nm}(\mathbf{k})$ and k -space local gap renders narrow ring-like structures enclosing the mBZ corners, in which \mathcal{G} is prominent and points radially inward/outward around κ/κ' . The distribution of \mathcal{G} dictates that of $[\partial_{\mathbf{k}} \times \mathcal{G}]_z$. The solid and dashed grey curves in Fig. 2(b) represent two energy contours with the former corresponding to a lower doping level. One observes

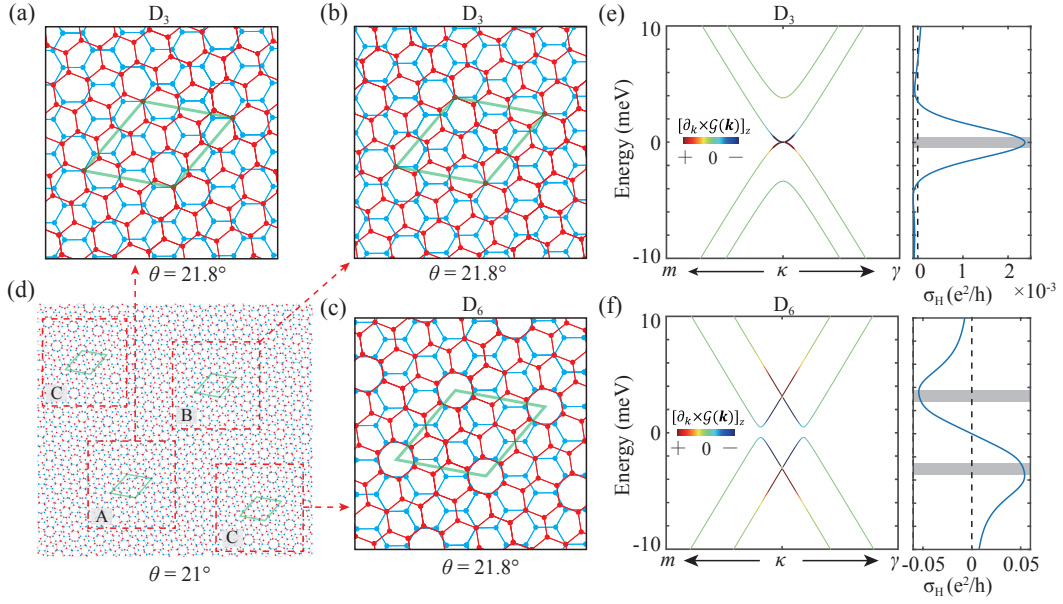


FIG. 3. (a-c) Three high-symmetry stacking registries for tBG with a commensurate twist angle $\theta = 21.8^\circ$. Lattice geometries with rotation center on an overlapping atomic site (a, b) and hexagonal center (c). (d) Schematic of the moiré pattern when the twist angle slightly deviates from 21.8° , here $\theta = 21^\circ$. Red squares marked by A, B and C are the local regions that resemble commensurate 21.8° patterns in (a), (b) and (c), respectively. (e, f) Low-energy band structures and intrinsic Hall conductivity of the two geometries [(a) and (b) are equivalent]. The shaded areas highlight energy windows $\sim \hbar\omega$ around band degeneracies where interband transitions, not considered here, may quantitatively affect the conductivity measured.

that $[\partial_{\mathbf{k}} \times \mathcal{G}]_z$ is negligible at lower energies, and it is dominated by positive values as the doping increases, thus the conductivity rises initially. When the doping level is higher, regions with $[\partial_{\mathbf{k}} \times \mathcal{G}]_z < 0$ start to contribute, thus the conductivity decreases after reaching a maximum.

Application to tBG. The second example is tBG. We focus on commensurate twist angles in the large angle limit in the main text [35], which possess moiré-lattice assisted strong interlayer tunneling via Umklapp processes [36]. This case is appealing because the Umklapp interlayer tunneling is a manifestation of discrete translational symmetry of moiré superlattice, which is irrelevant at small twist angles and not captured by the continuum model but plays important roles in physical contexts such as higher order topological insulator [37] and moiré excitons [38–40]. The Umklapp tunneling is strongest for the commensurate twist angles of $\theta = 21.8^\circ$ and $\theta = 38.2^\circ$, whose corresponding periodic moiré superlattices have the smallest lattice constant ($\sqrt{7}$ of the monolayer counterpart). Such a small moiré scale implies that the exact crystalline symmetry, which depends sensitively on fine details of rotation center, has critical influence on low-energy response properties.

To capture the Umklapp tunneling, we employ the tight-binding model [35]. Figures 3(a, b) and (c) show two distinct commensurate structures of tBG at $\theta = 21.8^\circ$ belonging to chiral point groups D_3 and D_6 , respectively. The atomic configurations in Figs. 3(a, b) are equivalent, which are constructed by twisting AA-

stacked bilayer graphene around an overlapping atom site, and that in Fig. 3(c) is obtained by rotating around a hexagonal center. Band structures of these two configurations are drastically different within a low-energy window of ~ 10 meV around the κ point [35]. Remarkably, despite large θ , we still get $\sigma_H \sim \mathcal{O}(0.001) e^2/h$ (D_3) and $\sim \mathcal{O}(0.1) e^2/h$ (D_6), which are comparable to those at small angles (cf. Fig. S1 in the Supplemental Material [41]). Such sizable responses can be attributed to the strong interlayer coupling enabled by Umklapp processes [26, 38–40]. Apart from different intensities, the Hall conductivities in the two stacking configurations have distinct energy dependence: In Fig. 3(e), σ_H shows a single peak centered at zero energy; In Fig. 3(f), it exhibits two antisymmetric peaks around zero. The peaks are centered around band degeneracies, and their profiles can be understood from the distribution of $[\partial_{\mathbf{k}} \times \mathcal{G}]_z$.

Figure 3(d) illustrates the atomic structure of tBG with a twist angle slightly deviating from $\theta = 21.8^\circ$, forming a supermoiré pattern. In short range, the local stacking geometries resemble the commensurate configurations at $\theta = 21.8^\circ$, while the stacking registries at different locales differ by a translation. Similar to the moiré landscapes in the small-angle limit, there also exist high-symmetry locales: Regions A and B enclose the D_3 structure, and region C contains the D_6 configuration. Position-dependent Hall response is therefore expected in such a supermoiré. As the intrinsic Hall signal from the D_6 configuration dominates [see Figs. 3(e) vs (f)], the net response mimics that in Fig. 3(f).

Discussion. We have uncovered the crossed nonlinear dynamical intrinsic Hall effect characteristic of layer hybridized electronic states in twisted bilayers, and elucidated its geometric origin in the k -space curl of interlayer BCP. It offers a new tool for rectification and frequency doubling in chiral vdW bilayers, and is sizable in tTMD and tBG. Here our focus is on the intrinsic effect, which can be evaluated quantitatively for each material and provides a benchmark for experiments. There may also be extrinsic contributions, similar to the side jump and skew scattering ones in anomalous Hall effect. They typically have distinct scaling behavior with the relaxation time τ from the intrinsic effect, hence can be distinguished from the latter in experiments [3, 5, 12, 42]. Moreover, they are suppressed in the clean limit $\omega\tau \gg 1$ [$(\omega\tau)^2 \gg 1$, more precisely] [12]. In high-quality tBG samples, $\tau \sim \text{ps}$ at room temperature [43]. Much longer τ can be obtained at lower temperatures. In fact, a recent theory explaining well the resistivity of tBG predicted $\tau \sim 10^{-8} \text{ s}$ at 10 K [44]. As such, high-quality tBG under low temperatures and sub-terahertz input ($\omega/2\pi = 0.1 \text{ THz}$) is located in the clean limit, rendering an ideal platform for isolating the intrinsic effect.

This work paves a new route to driving in-plane response by out-of-plane dynamical control of layered vdW structures [45]. The study can be generalized to other observables such as spin current and spin polarization, and the in-plane driving can be statistical forces, like temperature gradient. Such orthogonal controls rely critically on the nonconservation of layer pseudospin degree of freedom endowed by interlayer coupling, and constitute an emerging research field at the crossing of 2D vdW materials, layertronics, twistrionics and nonlinear electronics.

This work is supported by the Research Grant Council of Hong Kong (AoE/P-701/20, HKU SRFS2122-7S05), and the Croucher Foundation. W.Y. also acknowledges support by Tencent Foundation.

* These authors contributed equally to this work.

† cong Xiao@hku.hk

‡ wangyao@hku.hk

- [1] I. Sodemann and L. Fu, *Phys. Rev. Lett.* **115**, 216806 (2015).
- [2] Q. Ma, S.-Y. Xu, H. Shen, D. MacNeill, V. Fatemi, T.-R. Chang, A. M. Mier Valdivia, S. Wu, Z. Du, C.-H. Hsu, S. Fang, Q. D. Gibson, K. Watanabe, T. Taniguchi, R. J. Cava, E. Kaxiras, H.-Z. Lu, H. Lin, L. Fu, N. Gedik, and P. Jarillo-Herrero, *Nature* **565**, 337 (2019).
- [3] K. Kang, T. Li, E. Sohn, J. Shan, and K. F. Mak, *Nat. Mater.* **18**, 324 (2019).
- [4] Z. Z. Du, H.-Z. Lu, and X. C. Xie, *Nat. Rev. Phys.* **3**, 744 (2021).
- [5] S. Lai, H. Liu, Z. Zhang, J. Zhao, X. Feng, N. Wang, C. Tang, Y. Liu, K. S. Novoselov, S. A. Yang, and W.-b. Gao, *Nat. Nanotechnol.* **16**, 869 (2021).
- [6] J. Zhou, W. Zhang, Y.-C. Lin, J. Cao, Y. Zhou, W. Jiang, H. Du, B. Tang, J. Shi, B. Jiang, X. Cao, B. Lin, Q. Fu, C. Zhu, W. Guo, Y. Huang, Y. Yao, S. S. P. Parkin, J. Zhou, Y. Gao, Y. Wang, Y. Hou, Y. Yao, K. Suenaga, X. Wu, and Z. Liu, *Nature* **609**, 46 (2022).
- [7] Y. Zhang and L. Fu, *Proc. Natl. Acad. Sci. U.S.A.* **118**, e2100736118 (2021).
- [8] D.-F. Shao, S.-H. Zhang, G. Gurung, W. Yang, and E. Y. Tsymbal, *Phys. Rev. Lett.* **124**, 067203 (2020).
- [9] P. He, G. K. W. Koon, H. Isobe, J. Y. Tan, J. Hu, A. H. C. Neto, L. Fu, and H. Yang, *Nat. Nanotechnol.* **17**, 378 (2022).
- [10] J. Duan, Y. Jian, Y. Gao, H. Peng, J. Zhong, Q. Feng, J. Mao, and Y. Yao, *Phys. Rev. Lett.* **129**, 186801 (2022).
- [11] N. Nagaosa, J. Sinova, S. Onoda, A. H. MacDonald, and N. P. Ong, *Rev. Mod. Phys.* **82**, 1539 (2010).
- [12] Z. Z. Du, C. M. Wang, S. Li, H.-Z. Lu, and X. C. Xie, *Nat. Commun.* **10**, 3047 (2019).
- [13] E. Y. Andrei and A. H. MacDonald, *Nat. Mater.* **19**, 1265 (2020).
- [14] L. Balents, C. R. Dean, D. K. Efetov, and A. F. Young, *Nat. Phys.* **16**, 725 (2020).
- [15] D. M. Kennes, M. Claassen, L. Xian, A. Georges, A. J. Millis, J. Hone, C. R. Dean, D. N. Basov, A. N. Pasupathy, and A. Rubio, *Nat. Phys.* **17**, 155 (2021).
- [16] E. Y. Andrei, D. K. Efetov, P. Jarillo-Herrero, A. H. MacDonald, K. F. Mak, T. Senthil, E. Tutuc, A. Yazdani, and A. F. Young, *Nat. Rev. Mater.* **6**, 201 (2021).
- [17] C. N. Lau, M. W. Bockrath, K. F. Mak, and F. Zhang, *Nature* **602**, 41 (2022).
- [18] N. P. Wilson, W. Yao, J. Shan, and X. Xu, *Nature* **599**, 383 (2021).
- [19] E. C. Regan, D. Wang, E. Y. Paik, Y. Zeng, L. Zhang, J. Zhu, A. H. MacDonald, H. Deng, and F. Wang, *Nat. Rev. Mater.* **7**, 778 (2022).
- [20] D. Pesin and A. H. MacDonald, *Nat. Mater.* **11**, 409 (2012).
- [21] X. Xu, W. Yao, D. Xiao, and T. F. Heinz, *Nat. Phys.* **10**, 343 (2014).
- [22] F. Wu, T. Lovorn, E. Tutuc, I. Martin, and A. H. MacDonald, *Phys. Rev. Lett.* **122**, 086402 (2019).
- [23] H. Yu, M. Chen, and W. Yao, *Natl. Sci. Rev.* **7**, 12 (2020).
- [24] D. Zhai and W. Yao, *Phys. Rev. Lett.* **125**, 266404 (2020).
- [25] Y. Gao, Y. Zhang, and D. Xiao, *Phys. Rev. Lett.* **124**, 077401 (2020).
- [26] D. Zhai, C. Chen, C. Xiao, and W. Yao, *arXiv preprint arXiv:2207.14644* (2022).
- [27] D. Xiao, M.-C. Chang, and Q. Niu, *Rev. Mod. Phys.* **82**, 1959 (2010).
- [28] Y. Gao, S. A. Yang, and Q. Niu, *Phys. Rev. Lett.* **112**, 166601 (2014).
- [29] C. Xiao, H. Liu, J. Zhao, S. A. Yang, and Q. Niu, *Phys. Rev. B* **103**, 045401 (2021).
- [30] C. Xiao, H. Liu, W. Wu, H. Wang, Q. Niu, and S. A. Yang, *Phys. Rev. Lett.* **129**, 086602 (2022).
- [31] D. J. Thouless, *Phys. Rev. B* **27**, 6083 (1983).
- [32] D. Culcer and Q. Niu, *Phys. Rev. B* **74**, 035209 (2006).
- [33] C. Wang, Y. Gao, and D. Xiao, *Phys. Rev. Lett.* **127**, 277201 (2021).
- [34] H. Liu, J. Zhao, Y.-X. Huang, W. Wu, X.-L. Sheng, C. Xiao, and S. A. Yang, *Phys. Rev. Lett.* **127**, 277202 (2022).

- (2021).
- [35] P. Moon and M. Koshino, *Phys. Rev. B* **87**, 205404 (2013).
 - [36] E. J. Mele, *Phys. Rev. B* **81**, 161405 (2010).
 - [37] M. J. Park, Y. Kim, G. Y. Cho, and S. Lee, *Phys. Rev. Lett.* **123**, 216803 (2019).
 - [38] H. Yu, Y. Wang, Q. Tong, X. Xu, and W. Yao, *Phys. Rev. Lett.* **115**, 187002 (2015).
 - [39] K. L. Seyler, P. Rivera, H. Yu, N. P. Wilson, E. L. Ray, D. G. Mandrus, J. Yan, W. Yao, and X. Xu, *Nature* **567**, 66 (2019).
 - [40] L. Zhang, Z. Zhang, F. Wu, D. Wang, R. Gogna, S. Hou, K. Watanabe, T. Taniguchi, K. Kulkarni, T. Kuo, S. R. Forrest, and H. Deng, *Nat. Commun.* **11**, 1 (2020).
 - [41] See Supplemental Material for the effect in tBG with small twist angles.
 - [42] C. Xiao, H. Zhou, and Q. Niu, *Phys. Rev. B* **100**, 161403(R) (2019).
 - [43] L. Sun, Z. Wang, Y. Wang, L. Zhao, Y. Li, B. Chen, S. Huang, S. Zhang, W. Wang, D. Pei, H. Fang, S. Zhong, H. Liu, J. Zhang, L. Tong, Y. Chen, Z. Li, M. H. Rummeli, K. S. Novoselov, H. Peng, L. Lin, and Z. Liu, *Nat. Commun.* **12**, 2391 (2021).
 - [44] G. Sharma, I. Yudhistira, N. Chakraborty, D. Y. Ho, M. Al Ezzi, M. S. Fuhrer, G. Vignale, and S. Adam, *Nat. Commun.* **12**, 1 (2021).
 - [45] D. Zhai and W. Yao, *Nat. Sci.* **2**, e20210101 (2022).
 - [46] M. Koshino, N. F. Q. Yuan, T. Koretsune, M. Ochi, K. Kuroki, and L. Fu, *Phys. Rev. X* **8**, 031087 (2018).
 - [47] Z. Song, Z. Wang, W. Shi, G. Li, C. Fang, and B. A. Bernevig, *Phys. Rev. Lett.* **123**, 036401 (2019).

Supplemental Material

Cong Chen,^{1,2,*} Dawei Zhai,^{1,2,*} Cong Xiao,^{1,2,†} and Wang Yao^{1,2,‡}

¹*Department of Physics, The University of Hong Kong, Hong Kong, China*

²*HKU-UCAS Joint Institute of Theoretical and Computational Physics at Hong Kong, China*

Extra figures for tBG at small twist angles

Figure S4(a) shows the band structure of tBG with $\theta = 1.47^\circ$ obtained from the continuum model [46]. The central bands are well separated from higher ones, and show Dirac points at κ/κ' points protected by valley $U(1)$ symmetry and a composite operation of twofold rotation and time reversal $C_{2z}\mathcal{T}$ [47]. Degeneracies at higher energies can also be identified, for example, around ± 75 meV at the γ point. As the two Dirac cones from the two layers intersect around the same area, such degeneracies are usually accompanied by strong layer hybridization [see the color in the left panel of Fig. S4(a)]. Additionally, it is well-known that the two layers are strongly coupled when θ is around the magic angle ($\sim 1.08^\circ$), rendering narrow bandwidths for the central bands. As discussed in the main text, coexistence of strong interlayer hybridization and small energy separations is expected to contribute sharp conductivity peaks near band degeneracies, as shown in Fig. S4(a). In this case, the conductivity peak near the Dirac point can reach $\sim 0.1e^2/h$, while the responses around ± 0.08 eV are smaller at $\sim 0.01e^2/h$.

The above features are maintained when θ is enlarged, as illustrated in Figs. S4(b) and (c) using $\theta = 2.65^\circ$ and $\theta = 6.01^\circ$. Since interlayer coupling becomes weaker and the bands are more separated at low energies when θ increases, intensity of the conductivity drops significantly.

We stress that \mathcal{G} is not defined at degenerate points, and interband transitions may occur when energy separation satisfies $|\varepsilon_n - \varepsilon_m| \sim \hbar\omega$, the effects of which are not included in the current formulations. Consequently, the results around band degeneracies within energy $\sim \hbar\omega$ [shaded areas in Fig. S4] should be excluded.

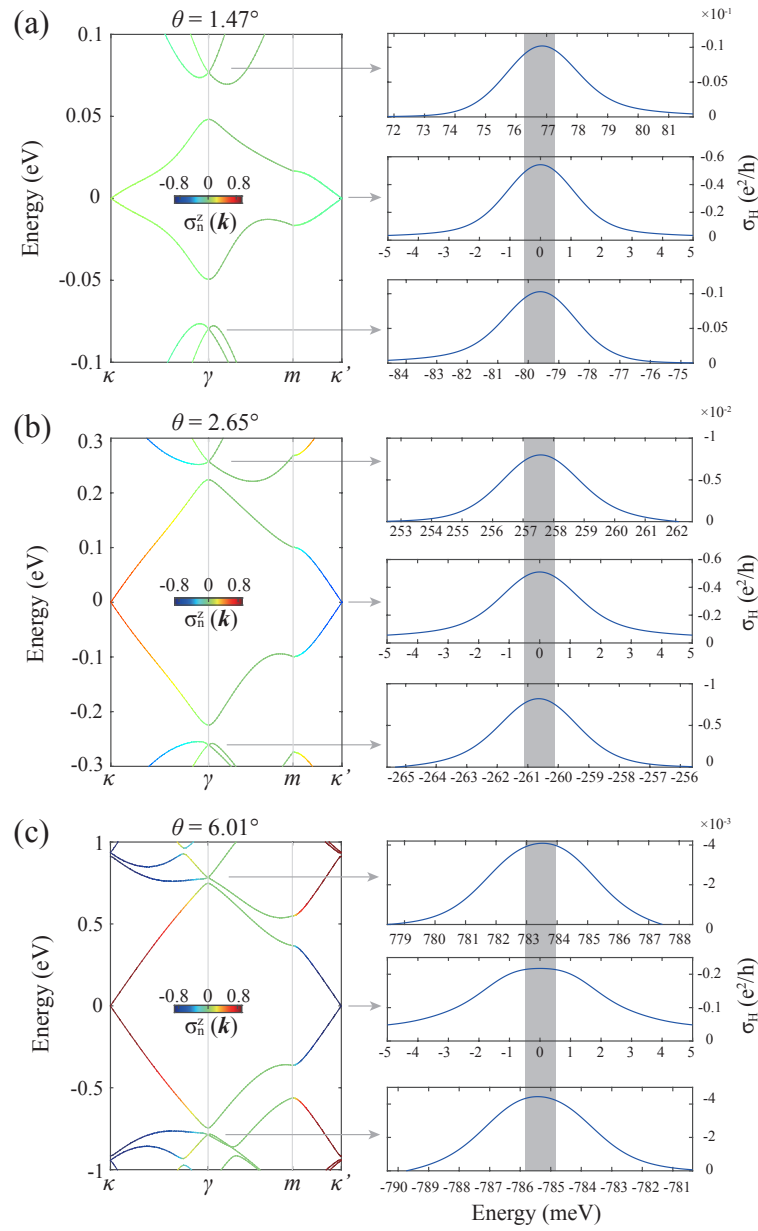


FIG. S4. Band structure and layer composition σ_n^z in +K valley of tBG (left panel) and the intrinsic Hall conductivity (right panel) at three different twist angle θ . The shaded areas highlight energy windows $\sim \hbar\omega$ around band degeneracies in which the conductivity results should not be considered. Here σ_H should be multiplied by a factor of 2 accounting for spin degeneracy.